ACS APPLIED ELECTRONIC MATERIALS

pubs.acs.org/acsaelm Article

Enhanced Neutron and γ-Ray Detection via ^{6}Li Substitution in Undoped and Tl-Doped Zero-Dimensional Perovskite $Cs_3Cu_2I_5$ Scintillators

Luis Stand,* Kimberly S. Pestovich, Ketaki Joshi, Xianfei Wen, Jason Hayward, Yauhen Tratsiak, Daniel Rutstrom, Myles Inniss, Charles L. Melcher, Jarek Glodo, Edgar Van Loef, and Mariya Zhuravleva

Cite This: https://doi.org/10.1021/acsaelm.4c02245 Read Online

ACCESS | Metrics & More | Article Recommendations | Supporting Information

ABSTRACT: Radiation detectors are crucial in a wide variety of research and commercial applications, such as oil and gas exploration, medical imaging, nuclear nonproliferation, and homeland security. Neutron and γ-ray detectors are fundamental components in portal monitors at ports and border crossings, bolstering national security against radiological threats. This study presents a dual-mode scintillator, undoped and Tl-doped ^{6}Li–$Cs_3Cu_2I_5$, and demonstrates its potential as a promising material for simultaneous thermal neutron and γ-ray detection. We explore the Bridgman growth of both undoped and thallium-doped Li → Cu and Li → Cs substitutional systems with various Li doping levels and assess their impact on scintillation properties. Under 662 keV γ-ray excitation, the undoped crystals had light yields up to 35,900 ph/MeV, with energy resolutions down to 4.5%. The Tl-doped crystals performed better than the undoped crystals, with light yields peaking at 65,900 ph/MeV and energy resolutions as low as 3.5%. When exposed to a moderated ^{252}Cf excitation source, our crystals had light yields between 102,900 and 167,200 photons per thermal neutron capture, with a full energy thermal neutron peak reaching 3 MeV in γ equivalent energy. Pulse shape discrimination studies reveal well-separated γ and neutron events, resulting in a figure-of-merit (FOM) as high as 3.7. These findings highlight the potential of Li-doped $Cs_3Cu_2I_5$ as a viable candidate for next-generation dual-mode scintillators.

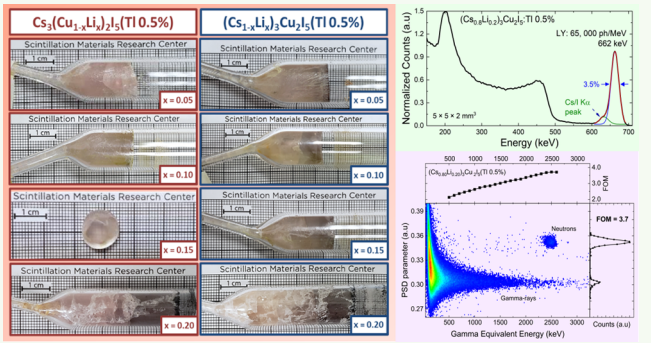

KEYWORDS: *single crystal, Bridgman growth, scintillator, neutron detection, pulse shape discrimination, perovskite*

1. INTRODUCTION

Single crystal scintillators are essential radiation sensors in various γ-ray and X-ray applications, including medical imaging, oil and gas exploration, high-energy physics, nuclear nonproliferation, and homeland security.[1−6] Neutron detectors, in particular, are critical for national security applications, as they are employed in radiation portal monitors at ports and border crossings to safeguard against smuggled nuclear materials and other radiological threats.[7] Traditional device designs consist of two independent detectors with scintillators like NaI(Tl) or PVT for γ-ray detection and ^{3}He-gas-filled proportional counters for thermal neutron detection. The global shortage of ^{3}He in the late 2000s highlighted a concerning dependence on this resource and sparked the pursuit of innovative neutron detection materials and methods as alternatives to traditional ^{3}He-based systems.[8,9] Consequently, dual-mode inorganic scintillators emerged as a promising alternative for neutron detection, leveraging neutron-sensitive materials capable of producing distinguishable γ and neutron responses that can be separated using pulse shape discrimination (PSD).[10−14] To explore scintillators with PSD capability, researchers have utilized two main strategies: (1) discover new scintillator compounds in which the neutron absorber isotope (^{10}B or ^{6}Li) is a constituent element such as Cs_2LiYCl_6(Ce), $Cs_2LiLaBr_{6-x}Cl_x$(Ce), $Tl_2Li(RE)Cl_6$, and $LiSr_2I_5$(Eu);[15−27] and (2) engineer existing compounds by partially replacing one of the constituent elements with the neutron absorber to form solid solutions, i.e., $Na_{1-x}Li_xI$ and $Cs_{1-x}Li_xI$.[28,29] Both approaches have demonstrated encouraging γ/neutron discrimination with the figure-of-merit (FOM) exceeding 2.

$Cs_3Cu_2I_5$ (CCI) is a versatile material with the potential to be used as a photodetector,[30] light-emitting diode,[31,32] and as a

Received: December 12, 2024
Revised: February 19, 2025
Accepted: February 20, 2025

Table 1. Compositions of the Li → Cu and Li → Cs Substitutional Systems Investigated in this Work

substitutional system	composition	Li (x) concentration	Tl-doping concentration (mol %)
Li → Cu	$Cs_3(Cu_{1-x}{}^6Li_x)_2I_5$	0.05,0.10	0
	$(Cs_{0.995}Tl_{0.05})_3(Cu_{1-x}{}^6Li_x)_2I_5$	0.05, 0.10, 0.15, 0.20	0.05
Li → Cs	$(Cs_{1-x}{}^6Li_x)_3Cu_2I_5$	0.05, 0.10	0
	$(Cs_{0.995-x}{}^6Li_xTl_{0.05})_3\ Cu_2I_5$	0.05, 0.10, 0.15, 0.20	0.05

scintillator material for radiation detection applications.[33−41] As a scintillator for γ-ray spectroscopy, CCI has light yields reaching 90,000 ph/MeV and energy resolution as low as 3.3% at 662 keV when doped with thallium.[38] The incorporation of ^{6}Li into the CCI matrix enabled this material to efficiently detect thermal neutrons via the ^{6}Li(n, α)t reaction. Thallium-doped ^{6}Li-CCI was introduced as a dual-mode scintillator by Glodo et al. in 2021.[42] Additional work by Wang et al. and Xiang et al. showed that undoped ^{6}Li (1 atom %)—CCI was sensitive to thermal neutrons and provided γ/neutron discrimination with an FOM of 2.25.[43,44]

In this work, we investigate the impact of incorporating higher ^{6}Li concentrations on the crystal growth and scintillation properties of $Cs_3Cu_2I_5$ and $Cs_3Cu_2I_5$:Tl. The crystal structure of CCI has four unique crystallographic sites where Li^+ can possibly be incorporated: (1) $[CsI_8]^{7-}$ (coordination number (CN) 8 = 1.74 Å), (2) $[CsI_9]^{8-}$ (Cs_{CN_9} = 1.78 Å),[45] (3) $[CuI_4]^{3-}$ (Li_{CN_4}: 0.60 Å),[45] and (4) $[Cu_2I_3]^-$ (Li_{CN_3}). Given the similar ionic radii of Li^+ (CN4: 0.59 Å)[45] and Cu^+ (CN4: 0.60 Å), Li^+ is more likely to replace Cu^+. However, Li^+ (CN8: 0.92 Å)[45] could also be substituted into the Cs^+ site (CN8: 1.74 Å). Therefore, we investigated undoped and Tl-doped crystals of both Li → Cu and Li → Cs substitutional systems with Li concentrations of 0.05, 0.10, 0.15, and 0.20 by growing single crystals using the vertical Bridgman method and characterizing phase formation and scintillation properties.

Our findings reveal excellent scintillation performance under γ and thermal neutron irradiation, including γ/neutron discrimination, with the best FOM of 3.7. These results highlight Li-CCI as a practical candidate for next-generation dual-mode scintillator detectors in national security applications.

2. EXPERIMENTAL METHODS

2.1. Crystal Growth. Single crystals of Li-CCI and Li-CCI:Tl were grown by using the Vertical Bridgman method in a two-zone transparent furnace. The compositions of the Li → Cu and Li → Cs systems are listed in Table 1. Note that in both systems, Tl^+ replaced Cs^+. Anhydrous 99.99% pure beads of CsI, ^{6}LiI, CuI, and TlI were mixed and loaded into 13 mm diameter quartz ampules. The loaded ampules were vacuum-dried at 100 °C for 12 h to remove any residual moisture and then sealed using an H_2−O_2 torch under a dynamic vacuum of at least 10^{-7} Torr. Before growth, several charge homogenization steps were performed by melting the raw materials at 720 °C for 24 h. The ampule was pulled at 0.2 mm/h through a thermal gradient of 18 °C/cm and then cooled to room temperature at 5 °C/h.

2.2. Sample Preparation. Samples of various sizes were cut and polished inside a N_2 glovebox and then placed inside a quartz container filled with mineral oil to protect them from moisture during the luminescence and scintillation measurements.

2.3. Phase Verification. Powder X-ray diffraction (PXRD) patterns were obtained with a PANalytical Empyrean 2-θ diffractometer. The powdered samples were loaded onto a zero-background silicon sample stage and then covered with a Kapton film to protect the powders from moisture during the measurement. Scans were collected from 10 to 70° 2-θ with a step size of 0.0131°. The measured PXRD pattern was matched to a reference using GSAS-II software to investigate the structure and phase purity.[46] $Cs_3(Cu_{1-x}{}^6Li_x)_2I_5$:Tl 0.5%, x = 0.15 was not measured.

2.4. Scintillation Characterization. Radioluminescence (RL) measurements were conducted at room temperature under continuous (35 keV, 0.1 mA) X-ray irradiation using a CMX003 X-ray generator. Emission spectra were collected over a wavelength range of 200−800 nm using a 150 mm focal length Acton SpectraPro-2150i monochromator.

The pulse height spectra with excitation from γ-ray-sealed sources were collected using a photomultiplier tube (PMT) connected to standard NIM electronic components consisting of a Canberra 2005 preamplifier, an Ortec 672 spectroscopy amplifier, and a Tukan 8K multichannel analyzer. The oil-filled quartz sample container was wrapped in Teflon and coupled to the PMT. Absolute light yield in photons per MeV (ph/MeV) was measured by the single photoelectron technique using a factory-measured quantum efficiency Hamamatsu R2059 PMT.[47] The pulse height spectra to determine the energy resolution (R) and scintillation nonproportionality (nPR) were collected using a Hamamatsu R6231−100 super bialkali PMT. The energy resolution was calculated from the ratio of the full width at half-maximum (FWHM) of the photopeak to its centroid (E): $R = \Delta E(\mathrm{FWHM})/E$. Nonproportionality was measured with a library of γ-ray sources, including ^{137}Cs, ^{133}Ba, ^{57}Co, and ^{241}Am. The light yield measured with 662 keV γ rays from the ^{137}Cs source was assigned to a value of 1.00, and the light yields measured at other energies were plotted relative to the 662 keV γ rays to illustrate deviations from proportionality.

For γ-neutron discrimination measurements, several thousands of scintillation traces under ^{137}Cs and ^{252}Cf irradiation were collected using an R6231−100 PMT. The crystal was surrounded by paraffin wax blocks to moderate the fast neutrons to thermal energy. A lead brick was placed between the ^{252}Cf source and the crystals for additional γ shielding. The PMT anode signal was digitized using a CAEN DT5720 desktop digitizer (sampling rate: 250 MS/s; ADC resolution: 14 bits). The digitized pulses were processed by using a custom Python code. The γ- and neutron-decay time constants were determined by fitting a two-component exponential function to the averaged traces. The γ-ray energy equivalent (GEE) and thermal neutron light yields were calculated by using 662 keV as the reference. For pulse shape discrimination (PSD) measurements, the traditional charge comparison method was used.[48] The PSD gate parameters were optimized (see the Supporting Information for details).

MCNP6.2[49] models were developed to evaluate the thermal neutron detection efficiency of Ø2.5 × 2.5 cm and Ø5 × 5 cm of Li-CCI(Tl), $Na_{x-1}{}^6Li_xI(Tl)$, $Cs_2{}^6LiLaBr_6(Ce)$ and $Cs_2{}^6LiYCl_6(Ce)$ detector-size crystals. In these models, the planar source of thermal neutrons impinged on the cylindrical side of the scintillator. The thermal neutron detection efficiency was defined as the ratio of thermal neutrons undergoing the (n,t) reaction with ^{6}Li to the total number of simulated source particles. The thermal detection efficiencies for both Li → Cu and Li → Cs substitutional systems were plotted as a function of ^{6}Li (atom %) concentration and compared to the detection efficiency of $Na_{x-1}{}^6Li_xI(Tl)$, $Cs_2{}^6LiLaBr_6(Ce)$, and $Cs_2{}^6LiYCl_6(Ce)$.

3. RESULTS AND DISCUSSION

3.1. Crystal Growth. Single crystals of undoped and Tl-doped Li → Cu and Li → Cs substitutional systems were

https://doi.org/10.1021/acsaelm.4c02245
ACS Appl. Electron. Mater. XXXX, XXX, XXX−XXX

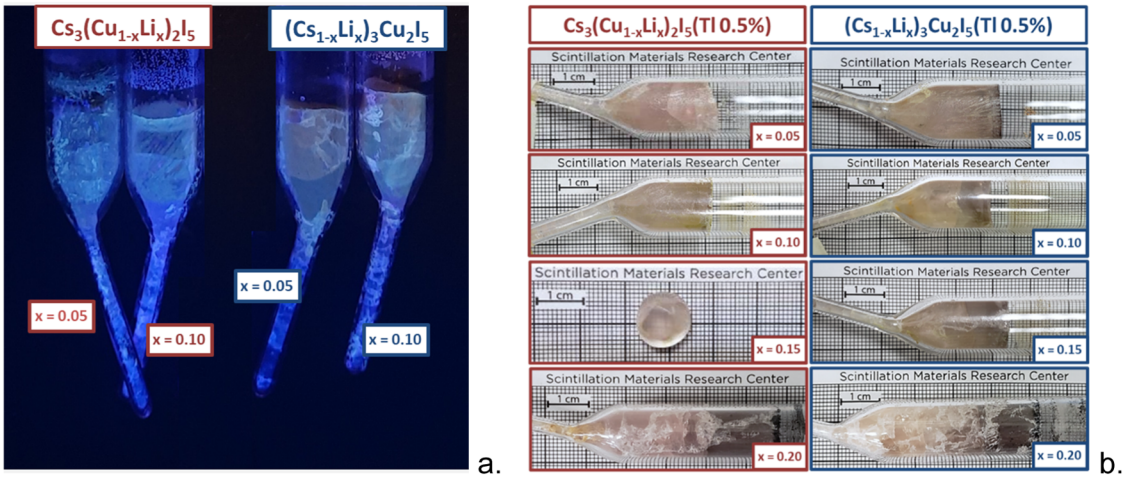

Figure 1. Ø12−13 mm single crystals of (a) undoped $Cs_3(Cu_{1-x}{}^6Li_x)_2I_5$ and $(Cs_{1-x}{}^6Li_x)_3Cu_2I_5$ inside the ampules under 254 nm excitation and (b)Tl-doped crystals inside the ampules under natural white light.

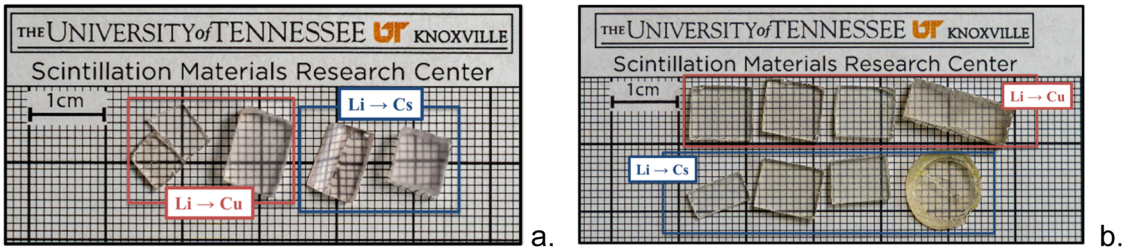

Figure 2. Polished samples of (a) undoped and (b) Tl-doped $Cs_3(Cu_{1-x}{}^6Li_x)_2I_5$ and $(Cs_{1-x}{}^6Li_x)_3Cu_2I_5$ under natural white light. Li concentrations in the samples increased from left to right.

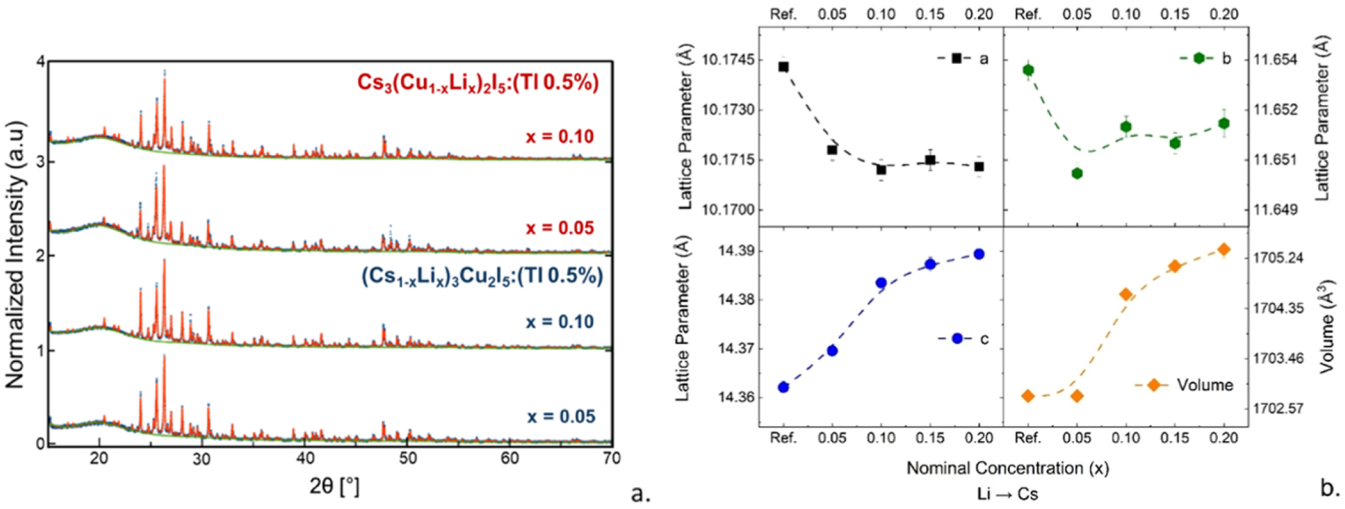

Figure 3. (a) Room temperature XRD patterns for selected Tl-doped $Cs_3(Cu_{1-x}{}^6Li_x)_2I_5$ and $(Cs_{1-x}{}^6Li_x)_3Cu_2I_5$ crystals (blue markers) compared to the calculated XRD pattern based on the $Cs_3Cu_2I_5$ structural model (red) from Hull and Berastegui.[55] (b) Rietveld refined lattice parameters for *a*, *b*, and *c* crystallographic directions as a function of Li (*x*) concentration for $(Cs_{1-x}{}^6Li_x)_3Cu_2I_5$:(Tl 0.5%).

successfully grown by the Vertical Bridgman technique. Figures 1 and 2 depict these crystals under UV excitation and natural light. All samples were transparent. The undoped crystals were predominantly pink, whereas the Tl-doped crystals had a yellow tint. It is important to note that the incorporation of Li did not influence the color of the crystals since similar color variations were observed in Li-free CCI crystals (Figure S1). The color inconsistencies are potentially related to variations in the quality of commercially available CuI precursor materials, such as purity, hydration level, trace oxygen impurity, and stoichiometry control of the Cu to I ratio. Most boules had small surface cracks penetrating less than a millimeter into the bulk of the crystals. These stress-induced cracks occured during the cooling phase as the crystal detached from the ampule wall.[50,51]

Li-CCI exhibits a peritectic behavior similar to pure CCI.[52−54] Consequently, the crystals, grown from stoichiometric melts, consisted of three visually distinct sections with

https://doi.org/10.1021/acsaelm.4c02245
ACS Appl. Electron. Mater. XXXX, XXX, XXX−XXX

Table 2. Lattice Parameters for Tl-Doped $Cs_3(Cu_{1-x}{}^6Li_x)_2I_5$ and $(Cs_{1-x}{}^6Li_x)_3Cu_2I_5$ Crystals Determined by Rietveld Refinement with GSAS-II[a]

	Li conc. (x)	a (Å)	b (Å)	c (Å)	volume (Å^3)
ref	0	10.1743(1)	11.6532(2)	14.3621(2)	1702.8(1)
Li → Cu	0.05	10.1731(3)	11.6520(1)	14.3684(5)	1703.1(2)
	0.10	10.1718(3)	11.6515(3)	14.3784(4)	1704.1(1)
	0.20	10.1716(4)	11.6513(2)	14.3881(3)	1705.2(3)
Li → Cs	0.05	10.1718(2)	11.6501(3)	14.3696(4)	1702.8(1)
	0.10	10.1712(3)	11.6515(4)	14.3849(4)	1704.8(1)
	0.15	10.1715(1)	11.6510(3)	14.3873(2)	1705.1(1)
	0.20	10.1713(2)	11.6516(1)	14.3894(3)	1705.4(2)

[a]Samples were cleaved from the middle section of the boules.

Table 3. Lattice Parameters for Tl-Doped $(Cs_{0.8}{}^6Li_{0.2})_3Cu_2I_5$ from the Seed, Bulk, and the Last-to-Freeze Regions Determined by Rietveld Refinement with GSAS-II

Li → Cs (x = 0.2)	a (Å)	b (Å)	c (Å)	volume (Å^3)
$Cs_3Cu_2I_5$:Tl (No Li)	10.1743(1)	11.6532(2)	14.3621(2)	1702.8(1)
Seed	10.1728(3)	11.6518(1)	14.3839(2)	1704.9(1)
Cone	10.1730(2)	11.6515(3)	14.3857(1)	1705.1(1)
middle	10.1713(2)	11.6516(1)	14.3894(3)	1705.4(2)
[a]LTF (Li−$Cs_3Cu_2I_5$)	10.1749(7)	11.6504(5)	14.4155(9)	1708.8(10)
[b]LTF (Li-$CsCu_2I_3$)	10.608 (7)	13.190 (5)	6.129(8)	857.7 (9)
$CsCu_2I_3$ ref	10.505 (1)	13.147(3)	6.072(2)	838.6(1)

[a]LTF ($Cs_3Cu_2I_5$)—0.40 phase fraction. [b]LTF ($CsCu_2I_3$)—0.60 phase fraction.

different phases. In our crystals, the CsI-rich phase was present at the bottom of the capillary. The bulk section of the crystal consisted of the desired orthorhombic-CCI phase. The remaining section was the last-to-freeze (LTF) and consisted of a mixture of Li−$Cs_3Cu_2I_5$:Tl and Li-$CsCu_2I_3$:Tl that solidified below the melting point of the desired compound. The size of the LTF did not change (∼2 mm) as the nominal lithium concentration increased from 0.05 to 0.15. This suggests that a significant amount of Li was incorporated into the bulk section with the desired orthorhombic-CCI phase. However, for x = 0.2, the LTF accounted for ∼40−50% of the crystal volume. The drastic increase in the LTF size indicates that the Li solubility in the CCI system was reached, and excess Li was rejected. Similar compositional stability was observed regardless of the assumed crystallographic site being substituted by Li^+.

Throughout our investigation into CCI and its variants, we found significant differences in crystal quality and scintillation performance due to phase inhomogeneities caused by unoptimized growth parameters. These secondary phase defects are either distributed uniformly throughout the crystal volume or segregated toward the outer edge of the crystal (Figures S2 and S3). The incongruent melting behavior of CCI makes the solid−liquid interface sensitive to small changes in growth parameters. For example, slowing down the pulling rate from 0.8 to 0.2 mm/h improved the optical quality, phase purity, and scintillation performance of CCI:Tl (Figures S4 and S5). Most reports of Bridgman-grown CCI, CCI:Tl, and Li-CCI show transparent boules but characterize the performance of only millimeter-thick pieces. This suggests that most crystals are not homogeneous. This is also evident by the significant differences in light yield, energy resolution, and decay times among published work. Some of these performance differences will be addressed in later sections of this work.

3.2. Phase Formation Investigation. The bulk of the crystals was phase pure, maintaining the orthorhombic *Pnma* (62) crystal structure of $Cs_3Cu_2I_5$.[54] Figure 3a illustrates powder X-ray diffraction patterns of selected Tl-doped compositions from the Li → Cu and Li → Cs substitutional systems, matched to the calculated pattern based on the crystallographic structural model of $Cs_3Cu_2I_5$ from Hull and Berastegui.[55] The lattice parameters from Rietveld refinement are given in Tables 2 and 3. A slight increase in unit cell volume was observed in both substitutional systems as we increased the nominal Li concentration from x = 0.05 to x = 0.20. This increase is attributed to the larger expansion of the "c" axis (∼0.027 Å) compared to the contractions of "a" (∼0.003 Å) and "b" (∼0.002 Å). However, if we consider ionic radii as the only determining factor, these results are unexpected. In the Li → Cu system, we expected the unit cell volume to remain nearly constant across all Li concentrations due to the nearly identical ionic radii of Li^+ and Cu^+ in the 4-fold coordinated site (0.59 Å for Li_{CN_4} vs 0.60 Å for Cu_{CN_4}[45]). In contrast, in the Li → Cs substitutional system, we expected the unit cell volume to decrease with increasing Li concentration due to the ionic radii Li^+ in the 8-fold coordinated site being half of the size of Cs^+ (1.74 Å for Cs_{CN_8} vs 0.92 Å for Li_{CN_4}[45]). Given our observations, it is very likely that Li^+ concentrations less than 5% incorporate into the energetically favorable Cu^+ site.[43] However, at higher Li concentrations, the peritectic behavior of CCI could allow Li^+ atoms to occupy both crystallographic sites to maintain compositional equilibrium, while some excess Li^+ occupies the interstitial site in the 8-coordinated Cs^+ site.

Since both systems experienced similar structural changes with the incorporation of Li, we decided to focus our structural studies on the Li → Cs system as it could possibly incorporate more Li compared to the Li → Cu system. Figure 3b illustrates the lattice parameter trends for the Li → Cs substitutional system. Samples were cleaved from the middle section of the boules. The unit cell volume increased from 1702.8 to 1705.4

https://doi.org/10.1021/acsaelm.4c02245
ACS Appl. Electron. Mater. XXXX, XXX, XXX−XXX

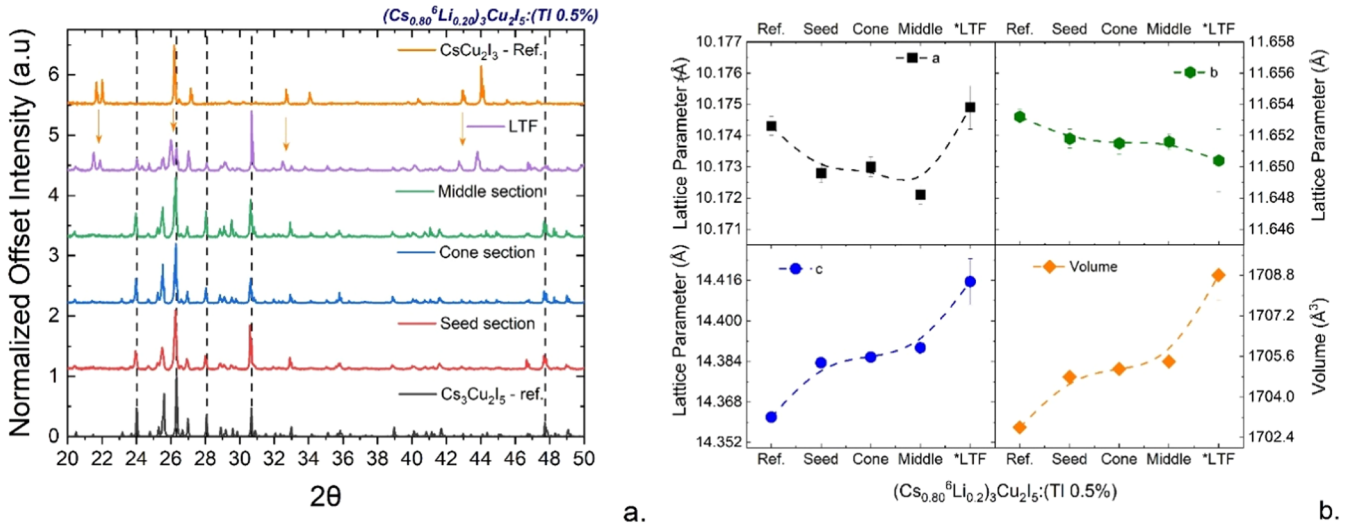

Figure 4. (a) XRD pattern of $Cs_{0.80}Li_{0.20}Cu_2I_5$:(Tl 0.5%) compared to the calculated XRD pattern based on the structural model from ICSD 150298—$Cs_3Cu_2I_5$[55] and ICSD 150305—$CsCu_2I_3$,[55] and (b) the refined structural parameters of $(Cs_{0.80}{}^6Li_{0.20})_3Cu_2I_5$:(Tl 0.5%) from various regions of interest across the boule.

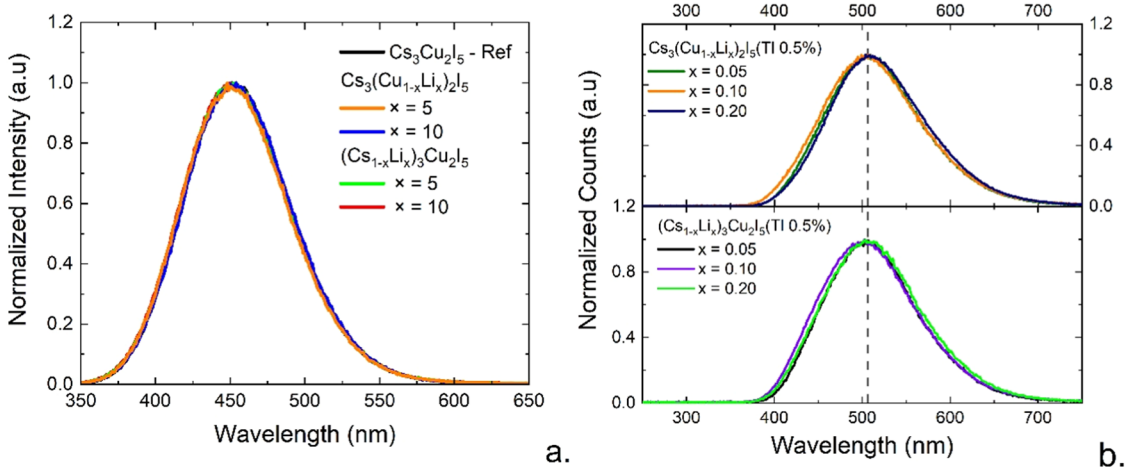

Figure 5. X-ray excited emission spectra of (a) undoped and (b) Tl-doped $Cs_3(Cu_{1-x}{}^6Li_x)_2I_5$ and $(Cs_{1-x}{}^6Li_x)_3Cu_2I_5$.

Å (2.6 Å) as the nominal Li^+ concentration increased from x = 0.5 to x = 0.20. Within this system, the largest change in volume (1.8 Å) occurred between x = 0.5 and 0.10, then it only increased by 0.6 Å as the Li^+ concentration increased from x = 0.10 to x = 0.20. Thus, it is likely that the unit cell volume plateaus around $0.10 \leq x < 0.15$, indicating that the Li^+ solubility limit may have been reached. This is supported by our growth observation, in which there was a significant increase in LTF size as the Li^+ concentration increased from x = 0.10 to x = 0.20.

We also investigated the phase uniformity of the crystal with the highest nominal concentration above the suggested solubility limit, x = 0.20, $(Cs_{1-x}Li_x)_3Cu_2I_5$:Tl 0.5%. The lattice parameters from the Rietveld refinement are listed in Table 3. As shown in Figure 4a,b, the seed, cone, and middle sections were single phases. The unit cell increased in volume from 1704.9 Å to 1705.4 Å due to Li^+ segregating along the growth direction. In this crystal, the average unit cell volume from the phase-pure section of the boule (1705.1 Å) is much closer to the unit cell volume of x = 0.10 (1704.8 Å) and x = 0.15 (1705.1 Å) than that of the Li−$Cs_3Cu_2I_5$ phase from the LTF section (1708.8 Å) (Figure 4b), confirming our expected solubility range. Similar trends were observed in the Li → Cu system; thus, we expect the nominal Li^+ concentration in the melt to be close to that in the Li → Cs system.

3.3. Scintillation Characterization. The incorporation of Li^+ did not significantly influence the X-ray excited emission of the undoped and Tl-doped crystals. Figure 5a,b depicts the radioluminescence emission spectra of Li-CCI and Li-CCI:Tl. Regardless of the substitutional system, the Tl-free crystals had a broad self-trapped exciton (STE) band centered at 452 nm,[43,44] and the Tl-doped crystals had a broad Tl-related band centered at 505 nm.[39]

The incorporation of Li^+ into undoped CCI did not significantly influence the scintillation light yield or energy resolution compared to that of the pure crystal. Figure 6a,b shows the ^{137}Cs spectra of ~0.7 cm^3 ($7 \times 7 \times 13$ mm^3) crystals from the Li → Cu and the Li → Cs substitutional systems. Regardless of the Li concentration and its intended substitutional site, the light yields ranged between 34,300 and 35,900 ph/MeV, with energy resolutions between 4.5 and 4.7% at 662 keV.

The performance of the crystals was also consistent across different volumes. To demonstrate this, we measured the

https://doi.org/10.1021/acsaelm.4c02245
ACS Appl. Electron. Mater. XXXX, XXX, XXX−XXX

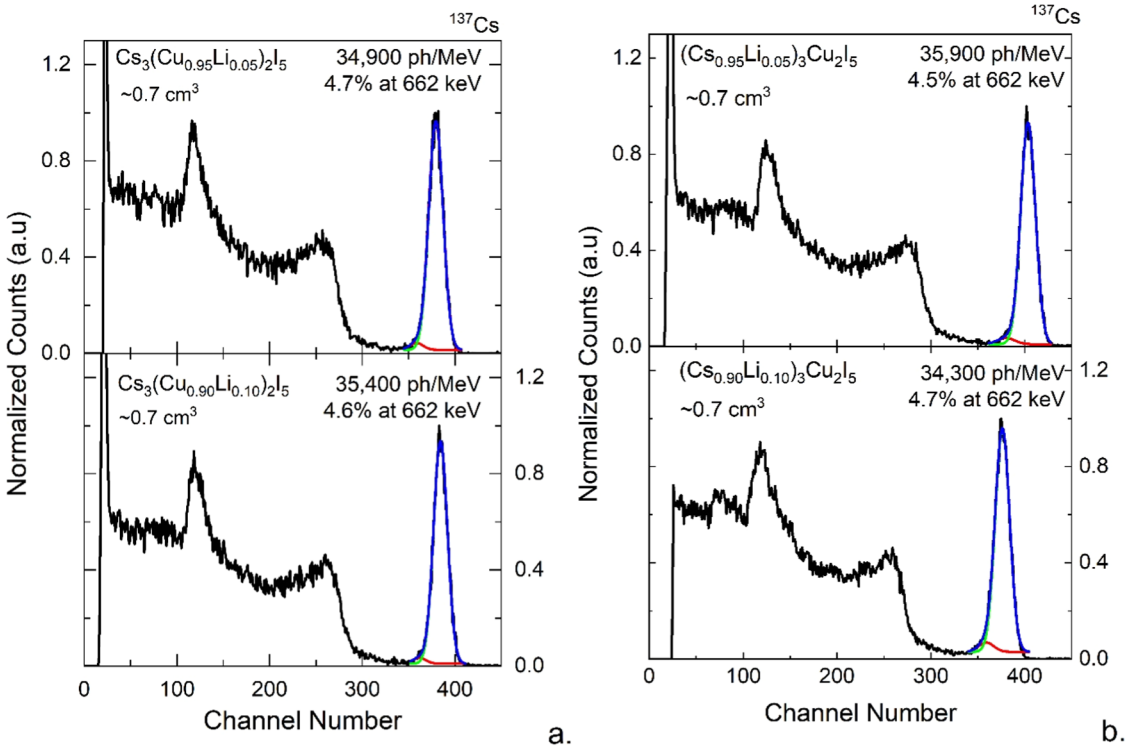

Figure 6. ^{137}Cs spectra of 7 × 7 × 13 mm^3 (0.7 cm^3) crystals: (a) $Cs_3(Cu_{1-x}{}^6Li_x)_2I_5$ and (b) $(Cs_{1-x}{}^6Li_x)_3Cu_2I_5$. Light yield and energy resolution at 662 keV are included in the legend.

energy resolution of 0.05, 0.25, and 0.7 cm^3 samples from the crystal with a high nominal Li concentration, $(Cs_{0.9}{}^6Li_{0.10})_3Cu_2I_5$. As shown in Figure 7, this crystal had excellent volumetric performance with energy resolutions between 4.6 and 4.7% at 662 keV as the sample volume increased.

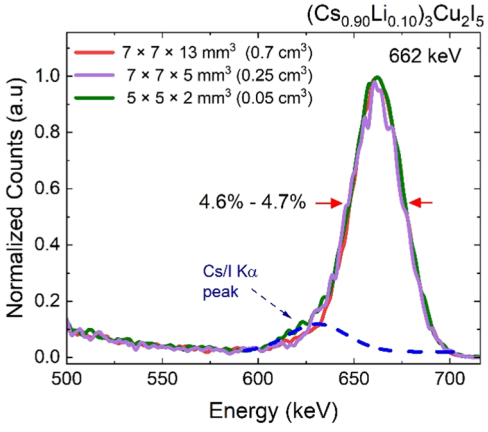

Figure 7. ^{137}Cs spectra highlighting the energy resolution at 662 keV of $(Cs_{0.90}{}^6Li_{0.10})_3Cu_2I_5$ crystals with different volumes.

Our results indicate that Li^+ incorporation into CCI had a different effect on scintillation properties compared with previous work. For small CCI crystals doped with Li 1 atom %, Wang et al. observed deterioration of the scintillation properties compared to Li-free CCI, i.e., light yield decreased by ∼10% to 30,000 ph/MeV and the energy resolution at 662 keV worsened from 4.4 to 4.8%.[43] In contrast, Xiang et al. reported an increase of light yield by ∼17% to 28,000 ph/MeV and an improvement of energy resolution at 662 keV from 7.2 to 5.25%.[44] In our work, the incorporation of Li^+ into CCI had no impact on the light yield and energy resolution in comparison to the Li-free CCI, and the best performance was 35,900 ph/MeV and energy resolutions of 4.5% at 662 keV measured for a 0.7 cm^3 $(Cs_{0.95}{}^6Li_{0.05})_3Cu_2I_5$ crystal. This is a significant improvement compared to the performance of much smaller crystals reported previously.

The light yield of Tl-doped Li-CCI crystals decreased by 25%, while the energy resolution at 662 keV remained unaffected compared to Li-free CCI:Tl. Figure 8a illustrates the light yield and energy resolution trends for 5 × 5 × 2 mm^3 (0.05 cm^3) and 7 × 7 × 5 mm^3 (0.25 cm^3) crystals from the Li → Cu and the Li → Cs substitutional systems. Regardless of the Li concentration and intended substitutional site, the light yield decreased from ∼82,000 ph/MeV to an average of ∼63,000 ph/MeV for equivalent Tl concentrations of 0.5%. The light yield remained relatively constant across the studied Li concentrations, ranging between 61,000 and 65,900 ph/MeV. The underlying cause of the reduced light output is not well understood. However, it is likely related to the slight increase in afterglow Li-CCI:Tl compared to Li-free CCI:Tl (Figure S6). This will be the subject of future investigation. The best energy resolution at 662 keV was 3.5% for smaller samples across all Li^+ concentrations in both substitutional systems. For the 0.25 cm^3 crystals, the energy resolution at 662 keV was between 3.8 and 4.1% at 662 keV. The performance of Li-CCI:Tl under γ irradiation surpasses that of CLYC:Ce (up to 20,000 ph/MeV, 3.6 to 4.4% at 662 keV)[18,21,27,56,57] and NaIL:Tl (40,000 ph/MeV and 6.5% at 662 keV),[28] while it is comparable to CLLBC:Ce (45,000 ph/MeV and 3.1−4.4% at 662 keV).[20,21,58]

Although CCI does not suffer from self-absorption, due to its large Stokes Shift,[31,32,35,40,59,60] other well-known factors

https://doi.org/10.1021/acsaelm.4c02245
ACS Appl. Electron. Mater. XXXX, XXX, XXX−XXX

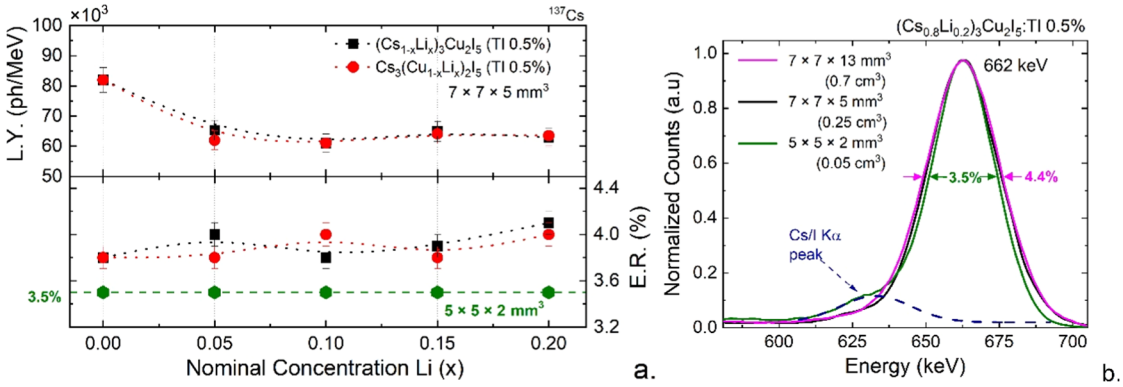

Figure 8. (a) Scintillation light yield (L. Y.) and energy resolution (E. R.) at 662 keV of 7 × 7 × 5 mm^3 Tl-doped $Cs_3(Cu_{1-x}{}^6Li_x)_2I_5$ and $(Cs_{1-x}{}^6Li_x)_3Cu_2I_5$ crystals with different Li (x) concentrations. The best E. R. (3.5%) measured for 5 × 5 × 2 mm^3 or smaller samples in both substitutional systems. (b) ^{137}Cs spectra highlighting the energy resolution at 662 keV for $(Cs_{0.8}{}^6Li_{0.2})_3Cu_2I_5$:Tl 0.5% with different volumes.

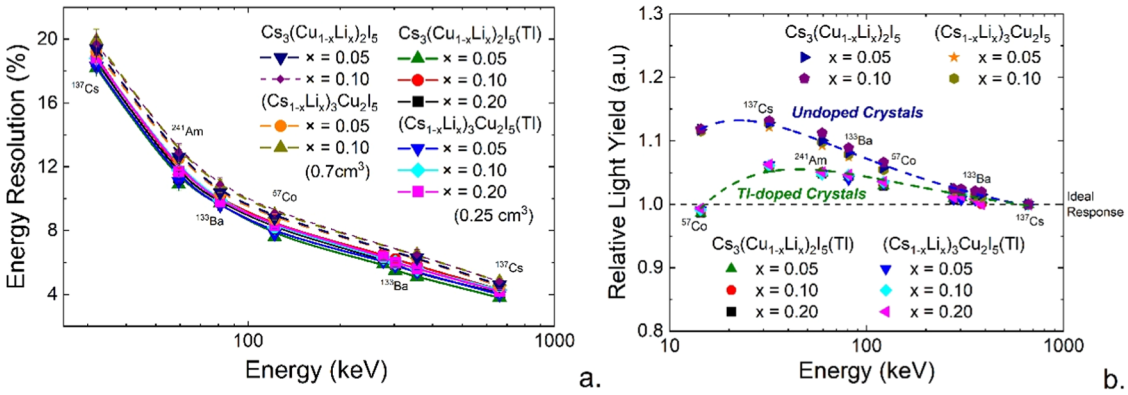

Figure 9. (a) Energy resolutions and (b) the relative light yield as a function of γ-ray energy for undoped and Tl-doped $Cs_3(Cu_{1-x}{}^6Li_x)_2I_5$ and $(Cs_{1-x}{}^6Li_x)_3Cu_2I_5$ with varying Li(x) concentrations.

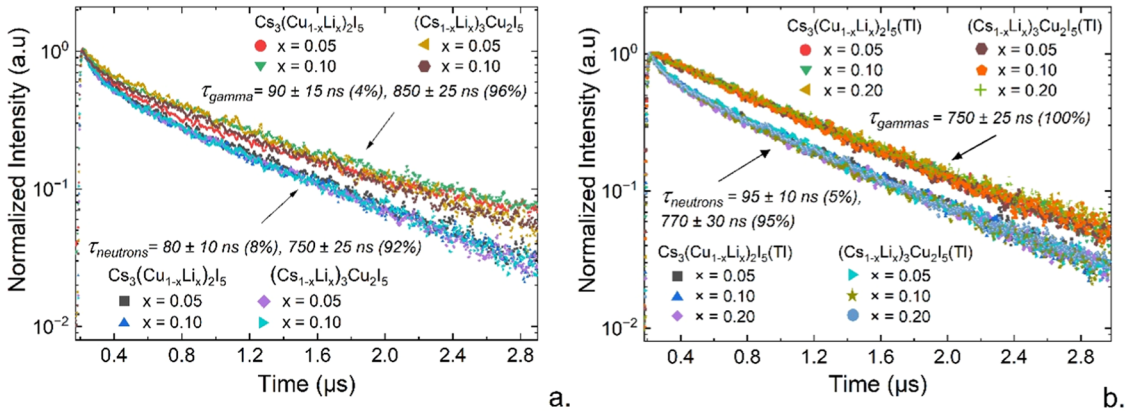

Figure 10. Scintillation decay time curves under γ-ray and neutron irradiation of (a) undoped and (b) Tl-doped $Cs_3(Cu_{1-x}{}^6Li_x)_2I_5$:Tl and $(Cs_{1-x}{}^6Li_x)_3Cu_2I_5$.

such as compositional inhomogeneities, impurities, and dopant segregation are also often responsible for the volumetric degradation of the energy resolution.[18,61,62] To further evaluate the volumetric performance in the Li → Cs system with the highest Li^+ nominal concentration, we compared the energy resolution of 0.05, 0.25, and 0.7 cm^3 crystals. The corresponding ^{137}Cs spectra are shown in Figure 8b. The energy resolution deteriorated from 3.5 to 4.4% as the volume increased from 0.05 cm^3 (5 × 5 × 2 mm^3) to 0.7 cm^3 (7 × 7 × 13 mm^3). Since no volumetric degradation of the energy resolution was observed for Tl-free Li-CCI (see Figure 7), we speculate that the observed degradation is likely caused by Tl inhomogeneities, i.e., inclusions, microinhomogeneities, and Tl-Li clusters. Similar effects have been observed in other Tl-doped crystals, such as CsI and NaI.[62−67]

The energy resolution versus energy and the light yield nonproportionality (nPR) curves are depicted in Figure 9a,b, respectively. The response to γ irradiation of the Li-containing crystals was similar compared to that of the Li-free crystals. The energy resolution and the light yield nonproportionality

https://doi.org/10.1021/acsaelm.4c02245
ACS Appl. Electron. Mater. XXXX, XXX, XXX−XXX

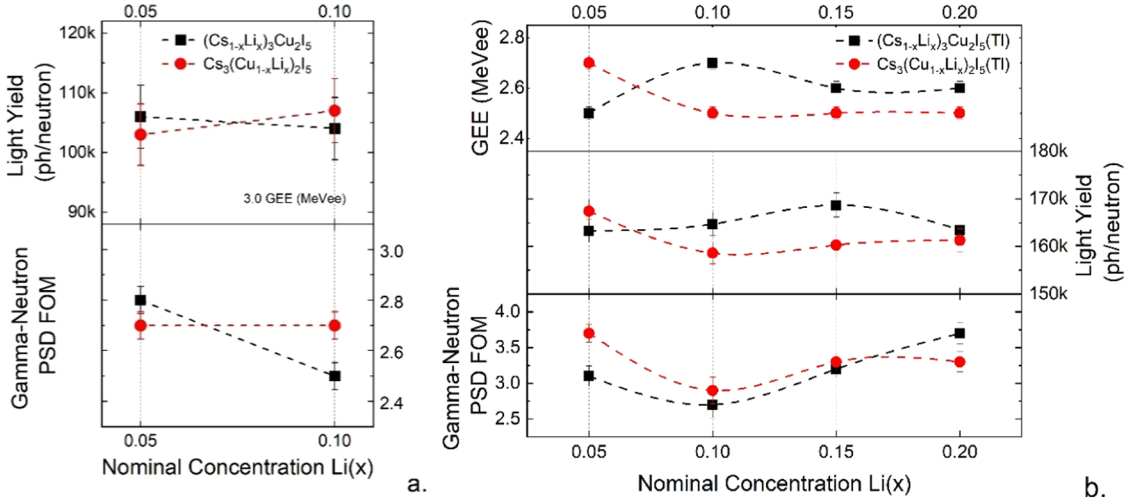

Figure 11. Neutron light yield and γ-neutron PSD figure-of-merit of (a) undoped and (b) Tl-doped $Cs_3(Cu_{1-x}{}^6Li_x)_2I_5$ and $(Cs_{1-x}{}^6Li_x)_3Cu_2I_5$. PSD, FOM, and ^{252}Cf spectra for all compositions are shown in the Supporting Information.

Table 4. Summary of Select Scintillation Properties of Undoped $Cs_3(Cu_{1-x}{}^6Li_x)_2I_5$ and $(Cs_{1-x}{}^6Li_x)_3Cu_2I_5$

	(x)	light yield γ (ph/MeV)	energy resolution (662 keV) (%)[a]	light yield n^0 (ph/neutron)	GEE n^0 (MeV)	FOM
$Cs_3(Cu_{1-x}{}^6Li_x)_2I_5$	0.05	34,900	4.7	104,700	3.0	2.7
	0.10	35,400	4.6	106,200	3.0	2.7
$(Cs_{1-x}{}^6Li_x)_3Cu_2I_5$	0.05	35,900	4.5	107,700	3.0	2.8
	0.10	34,300	4.7	102,900	3.0	2.5

[a]For 7 × 7 × 13 mm^3 crystals.

were not affected by the Li^+ concentration in either substitutional system. No double peaks in the pulse height spectra or sharp increases in energy resolution were observed across the energy resolution measured, indicating that the crystals' performance is uniform.[62] The undoped crystals have a highly nonproportional response with a pronounced "halide hump" that deviates from unity (ideal response) by 13% at approximately 30 keV. In contrast, the Tl-activated crystals have a more proportional response to γ-rays, with a much smaller halide hump deviating from the ideal response by only 4% at 30 keV (Figure 9b).

The incorporation of ^6Li had no influence on the scintillation decay time, but it enabled us to detect neutrons via the $^6Li(n,\alpha)t$ reaction. Figure 10a,b shows the average γ-ray and thermal neutron scintillation pulses for both substitutional systems. For Li-CCI, both the average γ-ray pulse and neutron scintillation pulses were fitted with a two-component exponential function, yielding time constants of 90 ± 15 ns (4%) and 850 ± 25 ns (96%) for γ-rays and 80 ± 10 ns (8%) and 750 ± 25 ns (92%) for neutrons. These results are consistent with decay observation made by Xiang et al.[44] However, Wang et al. reported that the γ-rays pulses were faster than neutron pulses.[43] For Li-CCI:Tl, the average γ-ray pulse was fitted with a single-component exponential function with a time constant of 750 ± 25 ns, while the average neutron pulse was fitted with a two-component exponential function with time constants of 95 ± 10 ns (5%) and 770 ± 30 ns (95%), as shown in Figure 10b.

In both Li-CCI and Li-CCI:Tl systems, the thermal neutron pulses are considerably faster than the γ-ray pulses. This is due to the ionization quenching effect.[4,21,28,68,69] This effect is a result of the high excitation density produced by α particles and tritons depositing their energy in a condensed ionization track, which causes STEs in close proximity to each other to lose their energy through a nonradiative transition (STE-STE annihilation).[4] In this study, the overall scintillation kinetics of Li-CCI and Li-CCI:Tl crystals were not affected by the nominal Li^+ concentration or its intended substitutional site when compared to the Li-free crystals.

The pulse shape differences between thermal neutron events and γ-ray events described in the previous section allow us to use the pulse shape discrimination (PSD) technique to differentiate between both events. In this method, a higher figure-of-merit (FOM) indicates better discrimination capability between γ and neutron events. Figure 11a shows the neutron light yield and γ-neutron PSD figure-of-merit (FOM) of undoped Li-CCI crystals from both substitutional systems. The thermal neutron peaks correspond to a γ-ray equivalent energy of 3 MeVee, resulting in a neutron light yield of 105,000 ± 10,000 photons per neutron. The neutron pulses were well separated from the γ-ray pulses, yielding an FOM ranging from 2.5 to 2.8, as shown in Figure 11a. These results show an improvement over the FOM of 2.27 shown for Li-CCI in previous works,[43,44] and commercially available CLLB:Ce (1.4) and CLLBC:Ce (2.5).[21,58] Table 4 summarizes the scintillation properties of undoped Li-CCI.

Tl-doping led to an improved neutron response compared to the undoped Li- CCI crystals. Figure 11b illustrates the neutron light yield and γ-neutron PSD FOM of a Tl-doped crystal for both substitutional systems. The thermal neutron peaks correspond to a γ-ray equivalent energy of approximately 2.6 MeVee. The neutron light yield of the Li → Cu system fluctuated around 162,100 ± 5000 photons per neutron, while the light yield of the Li → Cs system was between 165,100 ± 3000 photons per neutron. The PSD FOM of the Li → Cu system was consistently higher, ranging between 2.9 and 3.7,

https://doi.org/10.1021/acsaelm.4c02245
ACS Appl. Electron. Mater. XXXX, XXX, XXX−XXX

compared to that of Li → Cs, which ranged between 2.7 and 3.7. No trend between the Li^+ concentration and the thermal neutron response was observed. PSD, FOM, and ^{252}Cf pulse height spectra for all compositions investigated in this work are shown in the Supporting Information.

Figure 12a,b depicts the PSD scatter plots and FOM of crystals with the best performance under thermal neutron irradiation with the ^{252}Cf source, $(Cs_{0.80}{}^6Li_{0.20})_3Cu_2I_3$(Tl 0.5%) and $Cs_3(Cu_{0.95}{}^6Li_{0.05})_2I_3$(Tl 0.5%). Both crystals have an excellent FOM of 3.7 in the thermal neutron, comparable to CLYC:Ce (3.7) and NaIL:Tl (4.0).[18,21,28,57] Table 5 summarizes the scintillation properties of Li-CCI:Tl.

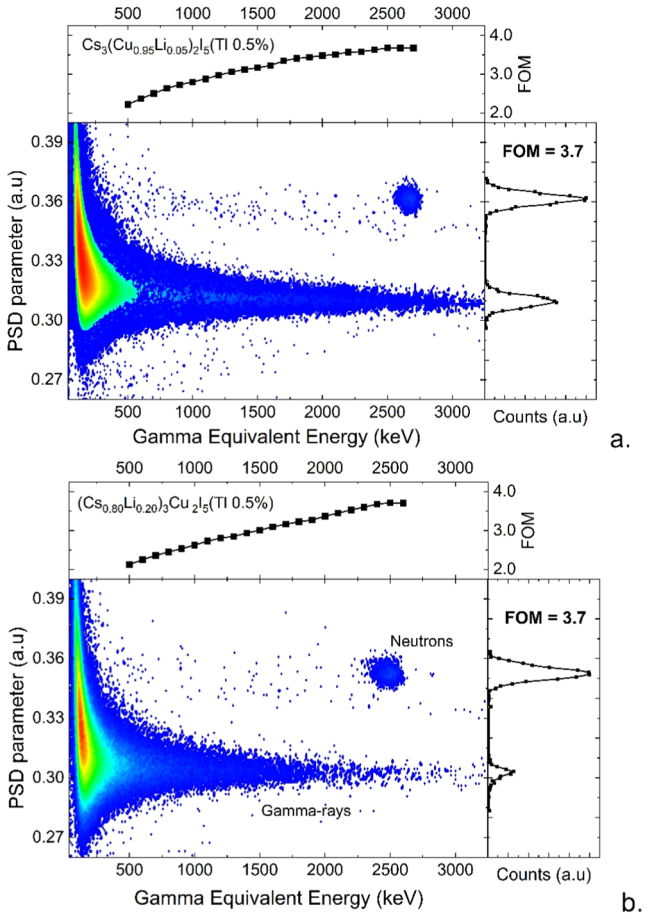

Figure 12. PSD scatter plot, FOM vs energy threshold and FOM in the thermal neutron range of (a) $Cs_3(Cu_{0.95}{}^6Li_{0.05})_2I_3$(Tl 0.5%) and (b) $(Cs_{0.80}{}^6Li_{0.20})_3Cu_2I_3$(Tl 0.5%) under thermal neutrons excitation from a ^{252}Cf source.

Figure 13a,13b shows thermal neutron detection efficiency MCNP calculations for Ø2.5 × 2.5 cm^3 and Ø5.0 × 5.0 cm^3 crystals from Tl-doped Li → Cu and Li → Cs substitutional systems compared to NaIL(Tl), CLLB(Ce), and CLYC(Ce). These sizes were chosen based on the typical size requirements for dual-mode hand-held detector systems.[70] The thermal neutron efficiencies of Li-CCI(Tl) and NaIL[28] increase with Li concentration due to the substitutional incorporation of Li. Both $Cs_2LiLaBr_6$(Ce) and Cs_2LiYCl_6(Ce) (CLYC(Ce)) have a fixed thermal neutron efficiency (shown as horizontal lines) because of the fixed Li^+ concentration due to their stoichiometry. In $Cs_3Cu_2I_5$, the Li → Cs system has a higher detection efficiency than the Li → Cu system due to the higher number of Cs atoms (3 vs 2) available for Li^+ substitution. The Li → Cs system achieves the detection efficiency of CLYC(Ce) at Li concentrations around 15 atom % for the small-size crystals and slightly above 12 atom % for the large-size crystals. The MCNP calculations refer to the actual Li^+ concentration in the final crystals rather than the nominal concentration of Li^+. Therefore, to reach the desired amount of Li^+ in the crystals, the Li^+ concentration in the melt should be adjusted to compensate for segregation and avoid phase separation during growth. In our case, a high Li^+ concentration causes phase instability, leading to phase separation. This is evidenced by the large multiphase last-to-freeze section and reduced single-phase Li-CCI(Tl) section of the crystal with a nominal concentration of 20%.

4. CONCLUSIONS

In this study, we successfully grew phase-pure, transparent single crystals of undoped and Tl-doped $Cs_3(Cu_{1-x}{}^6Li_x)_2I_5$ and $(Cs_{1-x}{}^6Li_x)_3Cu_2I_5$ using the vertical Bridgman technique.

Crystals in Li → Cu and Li → Cs substitutional systems with nominal Li^+ concentrations of x = 0.05, 0.10, and 0.15 were single-phase, similar to Li-free crystals. However, x = 0.20 caused phase separation, as evidenced by a large multiphase last-to-freeze section. Successful Li^+ incorporation in the crystals was confirmed by the change in the structural parameters as a function of the Li^+ concentration. According to Rietveld refinement, the "c" axis significantly expanded while the "a" and "b" axes contracted when the Li^+ concentration increased from x = 0.05 to x = 0.15. Due to the fact that only minimal changes are observed for x = 0.20, we concluded that the Li^+ solubility limit is below x = 0.15 regardless of the substitutional system.

Our results demonstrated that the incorporation of ^6Li enables $Cs_3Cu_2I_5$ to effectively detect thermal neutrons without compromising its γ-ray response. For undoped Li-CCI, the light yields ranged between 34,300 and 35,900 ph/MeV, with energy resolutions between 4.5 and 4.7% at 662

Table 5. Summary of Select Scintillation Properties of Tl-Doped $Cs_3(Cu_{1-x}{}^6Li_x)_2I_5$ and $(Cs_{1-x}{}^6Li_x)_3Cu_2I_5$

	(x)	light yield γ (ph/MeV)	energy resolution (662 keV)	light yield n^0 (ph/neutron)	GEE n^0 (MeV)	FOM
$Cs_3(Cu_{1-x}{}^6Li_x)_2I_5$(Tl 0.5%)	0.05	62,000	3.5% for 5 × 5 × 2 mm^3 crystals	167,400	2.7	3.7
	0.10	61,000		158,600	2.5	2.9
	0.15	64,100		160,300	2.5	3.3
	0.20	63,500		161,300	2.5	3.3
$(Cs_{1-x}{}^6Li_x)_3Cu_2I_5$(Tl 0.5%)	0.05	65,300	3.5% for 5 × 5 × 2 mm^3 crystals	163,300	2.5	3.1
	0.10	61,000		164,700	2.7	2.7
	0.15	65,900		168,700	2.6	3.2
	0.20	62,900		163,500	2.6	3.7

https://doi.org/10.1021/acsaelm.4c02245
ACS Appl. Electron. Mater. XXXX, XXX, XXX−XXX

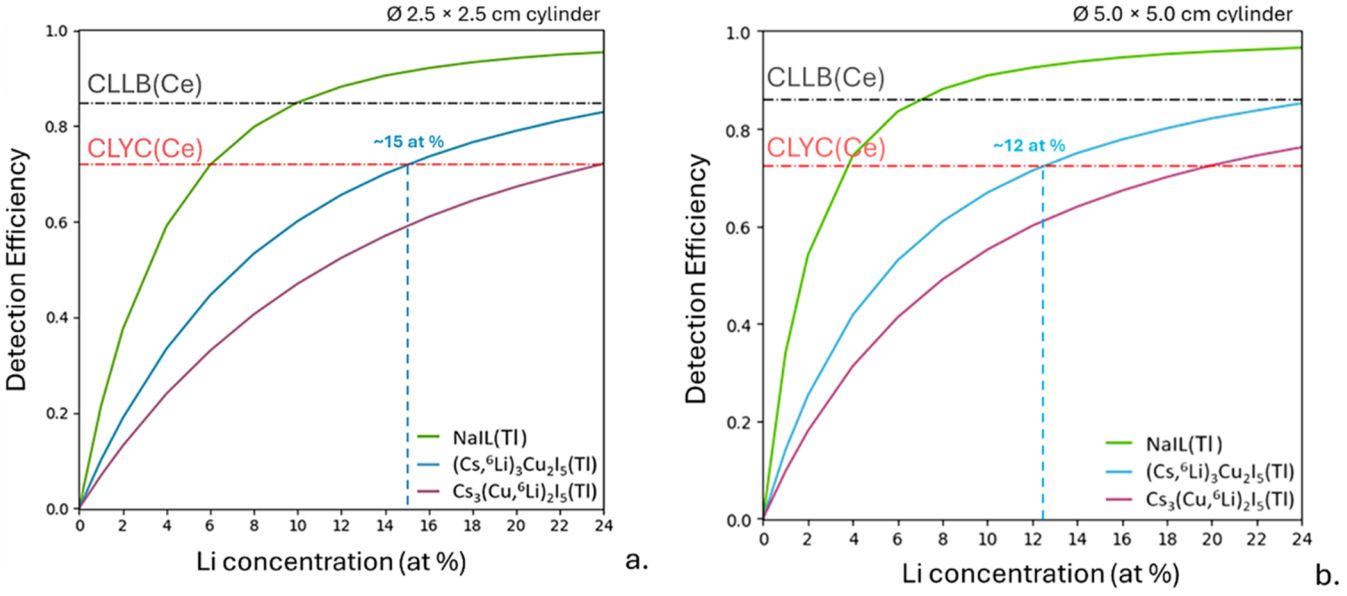

Figure 13. MCNP Simulated thermal neutron efficiency curves of (a) Ø2.5 × 2.5 cm and (b) Ø5.0 × 5.0 cm cylinders of $Cs_3(Cu_{1-x}{}^6Li_x)_2I_5(Tl)$ and $(Cs_{1-x}{}^6Li_x)_3Cu_2I_5(Tl)$ crystals as a function of ^6Li concentration compared to other benchmark scintillators.

keV. For Tl-doped crystals, the light yields were significantly higher, ranging from 61,000 to 65,900 ph/MeV, with energy resolutions between 3.5 and 4.1% at 662 keV. The Tl-doped crystals also exhibited superior thermal neutron response, with neutron light yields up to 168,700 photons per neutron and PSD FOM as high as 3.7. The enhanced performance of the Tl-doped crystals under both γ-ray and thermal neutron irradiation highlights their potential for high-performance dual-mode scintillator applications. These properties are comparable to those of commercially available scintillators such as $Cs_2LiYCl_6(Ce)$, $Cs_2LiLaBr_6(Ce)$, and NaIL(Tl). Additionally, we performed MCNP calculations to guide the compositional design to grow crystals for practical detector systems. The calculations recommended incorporating 12 to 15 atom % Li^+ to be competitive with state-of-the-art dual-mode scintillators.

Overall, our findings indicate that ^6Li- $Cs_3Cu_2I_5(Tl\ 0.5\%)$ is a promising dual-mode scintillator for nuclear nonproliferation applications. Future research will focus on optimizing crystal growth for detector-sized crystals of Tl-doped $(Cs_{1-x}{}^6Li_x)_3Cu_2I_5$ with Li^+ concentrations between 10 and 15%. These crystals are expected to achieve the required thermal neutron detection efficiency and excellent discrimination between γ-rays and thermal neutrons while maintaining outstanding performance under γ-ray excitation.

■ ASSOCIATED CONTENT

Supporting Information

The Supporting Information is available free of charge at https://pubs.acs.org/doi/10.1021/acsaelm.4c02245.

Growth observations and phase separation in $Cs_3Cu_2I_5$ crystals; the effect on scintillation properties; and PSD and FOM of undoped and Tl-doped $Cs_3(Cu_{1-x}Li_x)_2I_5$ and $(Cs_{1-x}\ Li_x)_3\ Cu_2I_5$ (PDF)

■ AUTHOR INFORMATION

Corresponding Author

Luis Stand − *Scintillation Materials Research Center, University of Tennessee, Knoxville, Tennessee 37996, United States; Department of Nuclear Engineering, University of Tennessee, Knoxville, Tennessee 37996, United States;* orcid.org/0000-0001-6846-8986; Email: lstand@vols.utk.edu

Authors

Kimberly S. Pestovich − *Scintillation Materials Research Center, University of Tennessee, Knoxville, Tennessee 37996, United States; Department of Material Science and Engineering, University of Tennessee, Knoxville, Tennessee 37996, United States*

Ketaki Joshi − *Department of Nuclear Engineering, University of Tennessee, Knoxville, Tennessee 37996, United States*

Xianfei Wen − *Department of Nuclear Engineering, University of Tennessee, Knoxville, Tennessee 37996, United States*

Jason Hayward − *Department of Nuclear Engineering, University of Tennessee, Knoxville, Tennessee 37996, United States*

Yauhen Tratsiak − *Scintillation Materials Research Center, University of Tennessee, Knoxville, Tennessee 37996, United States;* orcid.org/0000-0002-1432-1054

Daniel Rutstrom − *Scintillation Materials Research Center, University of Tennessee, Knoxville, Tennessee 37996, United States; Department of Material Science and Engineering, University of Tennessee, Knoxville, Tennessee 37996, United States*

Myles Inniss − *Radiation Monitoring Devices, Inc., Dynasil Corporation of America, Watertown, Massachusetts 02472, United States*

Charles L. Melcher − *Scintillation Materials Research Center, University of Tennessee, Knoxville, Tennessee 37996, United States; Department of Nuclear Engineering and Department of Material Science and Engineering, University of Tennessee, Knoxville, Tennessee 37996, United States*

Jarek Glodo − *Radiation Monitoring Devices, Inc., Dynasil Corporation of America, Watertown, Massachusetts 02472, United States*

https://doi.org/10.1021/acsaelm.4c02245
ACS Appl. Electron. Mater. XXXX, XXX, XXX−XXX

Edgar Van Loef − *Radiation Monitoring Devices, Inc., Dynasil Corporation of America, Watertown, Massachusetts 02472, United States*

Mariya Zhuravleva − *Scintillation Materials Research Center, University of Tennessee, Knoxville, Tennessee 37996, United States; Department of Material Science and Engineering, University of Tennessee, Knoxville, Tennessee 37996, United States*

Complete contact information is available at: https://pubs.acs.org/10.1021/acsaelm.4c02245

Notes

DISCLAIMER This report was prepared as an account of work sponsored by an agency of the United States Government. Neither the United States Government nor any agency thereof, nor any of their employees, makes any warranty, express or implied, or assumes any legal liability or responsibility for the accuracy, completeness, or usefulness of any information, apparatus, product, or process disclosed, or represents that its use would not infringe privately owned rights. Reference herein to any specific commercial product, process, or service by trade name, trademark, manufacturer, or otherwise does not necessarily constitute or imply its endorsement, recommendation, or favoring by the United States Government or any agency thereof. The views and opinions of authors expressed herein do not necessarily state or reflect those of the United States Government or any agency thereof.

The authors declare no competing financial interest.

■ ACKNOWLEDGMENTS

This material is based on work supported in part by the Department of Energy National Nuclear Security Administration through the Nuclear Science and Security Consortium under Award Number DE-NA-0003996. XRD was performed at the Institute for Advanced Materials & Manufacturing (IAMM) Diffraction Facility, located at the University of Tennessee, Knoxville.

■ ABBREVIATIONS

CCI, $Cs_3Cu_2I_5$, cesium copper iodide; FOM, figure-of-merit; PSD, pulse shape discrimination; FWHM, full width half-maximum

■ REFERENCES

(1) Nikl, M. Scintillation detectors for x-rays. *Meas. Sci. Technol.* **2006**, *17* (4), No. R37.

(2) Lecoq, P. Development of new scintillators for medical applications. *Nucl. Instrum. Methods Phys. Res., Sect. A* **2016**, *809*, 130−139.

(3) Lecoq, P.; Gektin, A.; Korzhik, M. *Inorganic Scintillators for Detector Systems: Physical Principles and Crystal Engineering*; Springer, 2016.

(4) Rodnyi, P. A. *Physical Processes in Inorganic Scintillators*; CRC Press, 1997.

(5) Ellis, M. E.; Duroe, K.; Kendall, P. A. Pulse-shape discrimination scintillators for homeland security applications. *Int. J. Mod. Phys.: Conf. Ser.* **2016**, *44*, No. 1660214.

(6) Nelson, K. E.; Gosnell, T. B.; Knapp, D. A. *The Effect of Gamma-Ray Detector Energy Resolution on the Ability to Identify Radioactive Sources*; Lawrence Livermore National Lab. (LLNL): Livermore, CA (United States), 2009.

(7) Kouzes, R. T. *The ^{3}He Supply Problem*, PNNL-18388; Pacific Northwest National Laboratory, 2009.

(8) Committee on Science and Technology. *Caught by Surprise: Causes and Consequences of the Helium-3 Supply Crisis*; US Government Publishing Office, 2011.

(9) Office, G. A. *Weaknesses in DOE's Management of Helium-3 Delayed the Federal Response to a Critical Supply Shortage*; Congressional Research Service, 2011.

(10) Winyard, R. A.; Lutkin, J. E.; McBeth, G. W. Pulse shape discrimination in inorganic and organic scintillators. I. *Nucl. Instrum. Methods* **1971**, *95* (1), 141−153.

(11) Winyard, R. A.; McBeth, G. W. Pulse shape discrimination in inorganic and organic scintillators, II. *Nucl. Instrum. Methods* **1972**, *98* (3), 525−533.

(12) Alexander, T. K.; Goulding, F. S. An amplitude-insensitive system that distinguishes pulses of different shapes. *Nucl. Instrum. Methods* **1961**, *13*, 244−246.

(13) Roush, M. L.; Wilson, M. A.; Hornyak, W. F. Pulse shape discrimination. *Nucl. Instrum. Methods* **1964**, *31* (1), 112−124.

(14) Sperr, P.; Spieler, H.; Maier, M. R.; Evers, D. A simple pulse-shape discrimination circuit. *Nucl. Instrum. Methods* **1974**, *116* (1), 55−59.

(15) Hawrami, R.; Ariesanti, E.; Burger, A.; Neely, E.; Glodo, J.; Pandian, L.; Ji, C.; Stepanoff, S.; Wolfe, D. E.; Liang, F. Characterization of large diameter dual-mode cerium-doped Tl2LiYCl6 advanced scintillator. *Nucl. Instrum. Methods Phys. Res., Sect. A* **2023**, *1056*, No. 168626.

(16) Hawrami, R.; Ariesanti, E.; Wei, H.; Finkelstein, J.; Glodo, J.; Shah, K. Tl2LiYCl6: Large Diameter, High Performing Dual Mode Scintillator. *Cryst. Growth Des.* **2017**, *17* (7), 3960−3964.

(17) Hawrami, R.; Pandian, L. S.; Ariesanti, E.; Glodo, J.; Finkelstein, J.; Tower, J.; Shah, K. $Cs_2LiLa(Br,Cl)_6$ Crystals for Nuclear Security Applications. *IEEE Trans. Nucl. Sci.* **2016**, *63* (2), 509−512.

(18) Glodo, J.; Hawrami, R.; Shah, K. S. Development of Cs2LiYCl6 scintillator. *J. Cryst. Growth* **2013**, *379*, 73−78.

(19) Shirwadkar, U.; Hawrami, R.; Glodo, J.; van Loef, E.; Shah, K. S. In *Novel Scintillation Material Cs2LiLaBr6−xClx:Ce for Gamma-Ray and Neutron Spectroscopy*, 2012 IEEE Nuclear Science Symposium and Medical Imaging Conference Record (NSS/MIC); IEEE, 2012; pp 1963−1967.

(20) Shirwadkar, U.; Glodo, J.; van Loef, E. V.; Hawrami, R.; Mukhopadhyay, S.; Churilov, A.; Higgins, W. M.; Shah, K. S. Scintillation properties of Cs2LiLaBr6 (CLLB) crystals with varying Ce3+ concentration. *Nucl. Instrum. Methods Phys. Res., Sect. A* **2011**, *652* (1), 268−270.

(21) Glodo, J.; Loef, Ev.; Hawrami, R.; Higgins, W. M.; Churilov, A.; Shirwadkar, U.; Shah, K. S. Selected Properties of Cs_2LiYCl_6, $Cs_2LiLaCl_6$, and $Cs_2LiLaBr_6$ Scintillators. *IEEE Trans. Nucl. Sci.* **2011**, *58* (1), 333−338.

(22) van Loef, E. V. D.; Dorenbos, P.; van Eijk, C. W. E.; Krämer, K. W.; Güdel, H. U. Scintillation and spectroscopy of the pure and Ce3+-doped elpasolites: Cs2LiYX6 (X = Cl, Br). *J. Phys.: Condens. Matter* **2002**, *14* (36), No. 8481.

(23) Soundara-Pandian, L.; Hawrami, R.; Glodo, J.; Ariesanti, E.; Loef, E. V. v.; Shah, K. Lithium Alkaline Halides—Next Generation of Dual Mode Scintillators. *IEEE Trans. Nucl. Sci.* **2016**, *63* (2), 490−496.

(24) Hawrami, R.; Ariesanti, E.; Pandian, L. S.; Glodo, J.; Shah, K. S. In *Tl2LiLaBr6:Ce and Tl2LiYCl6:Ce: New Elpasolite Scintillators.*, 2015 IEEE Nuclear Science Symposium and Medical Imaging Conference (NSS/MIC); IEEE, 2015; pp 1−3.

(25) Kim, H. J.; Rooh, G.; Park, H.; Kim, S. Luminescence and scintillation properties of the new Ce-doped Tl2LiGdCl6 single crystals. *J. Lumin.* **2015**, *164*, 86−89.

(26) Rooh, G.; Kim, H. J.; Jang, J.; Kim, S. Scintillation characterizations of Tl2LiLuCl6: Ce3+ single crystal. *J. Lumin.* **2017**, *187*, 347−351.

(27) Combes, C. M.; Dorenbos, P.; van Eijk, C. W. E.; Krämer, K. W.; Güdel, H. U. Optical and scintillation properties of pure and

Ce3+-doped Cs2LiYCl6 and Li3YCl6:Ce3+ crystals. *J. Lumin.* **1999**, *82* (4), 299−305.
(28) Yang, K.; Menge, P. R.; Ouspenski, V. Li Co-Doped NaI:Tl (NaIL)—A Large Volume Neutron-Gamma Scintillator With Exceptional Pulse Shape Discrimination. *IEEE Trans. Nucl. Sci.* **2017**, *64* (8), 2406−2413.
(29) Nagarkar, V. V.; Ovechkina, E.; Bhandari, H.; Miller, S. R.; Marton, Z.; Glodo, J.; Soundara-Pandian, L.; Mengesha, W.; Gerling, M.; Brubaker, E. In *Lithium Alkali Halides—New Thermal Neutron Detectors with n-γ Discrimination*, 2013 IEEE Nuclear Science Symposium and Medical Imaging Conference (2013 NSS/MIC); IEEE, 2013; pp 1−4.
(30) Zhang, Z.-X.; Li, C.; Lu, Y.; Tong, X.-W.; Liang, F.-X.; Zhao, X.-Y.; Wu, D.; Xie, C.; Luo, L.-B. Sensitive Deep Ultraviolet Photodetector and Image Sensor Composed of Inorganic Lead-Free Cs3Cu2I5 Perovskite with Wide Bandgap. *J. Phys. Chem. Lett.* **2019**, *10* (18), 5343−5350.
(31) Zhang, F.; Zhao, Z.; Chen, B.; Zheng, H.; Huang, L.; Liu, Y.; Wang, Y.; Rogach, A. L. Strongly Emissive Lead-Free 0D Cs3Cu2I5 Perovskites Synthesized by a Room Temperature Solvent Evaporation Crystallization for Down-Conversion Light-Emitting Devices and Fluorescent Inks. *Adv. Opt. Mater.* **2020**, *8* (8), No. 1901723.
(32) Jun, T.; Sim, K.; Iimura, S.; Sasase, M.; Kamioka, H.; Kim, J.; Hosono, H. Lead-Free Highly Efficient Blue-Emitting Cs3Cu2I5 with 0D Electronic Structure. *Adv. Mater.* **2018**, *30* (43), No. 1804547.
(33) Zheng, R.; Wang, L.; Liu, Y.; Chen, J.; Xiao, P.; Xie, Q. Scintillation properties of Cs3Cu2I5:Tl crystals grown by Cz, EFG and Bridgman methods with a multifunctional melt growth furnace. *J. Cryst. Growth* **2024**, *627*, No. 127512.
(34) Gao, Q.; Wang, Q.; Li, W.; Gao, A.; Korzhik, M.; Kurosawa, S.; Ren, G.; Wu, Y. Effects of rare earth codoping on the optical and scintillation properties of Cs3Cu2I5:Tl single crystals. *J. Cryst. Growth* **2024**, *636*, No. 127717.
(35) Chatterjee, S.; Mukherjee, P.; Sen, A.; Sen, P. Evidence of Short-Lived High-Energy Emissive State and Triplet Character of the Self-Trapped Exciton in Cs3Cu2I5 Perovskite. *J. Phys. Chem. Lett.* **2024**, *15* (15), 4191−4196.
(36) Tratsiak, Y.; Stand, L.; Lalk, R.; Zhuravleva, M.; Melcher, C. L. Temperature-dependent luminescence in pure and In+-Activated Cs3Cu2I5 single crystals. *J. Lumin.* **2023**, *263*, No. 119952.
(37) Yao, Q.; Li, J.; Li, X.; Zheng, X.; Wang, Z.; Tao, X. High-Quality Cs3Cu2I5 Single-Crystal is a Fast-Decaying Scintillator. *Adv. Opt. Mater.* **2022**, *10* (23), No. 2201161.
(38) Stand, L.; Rutstrom, D.; Koschan, M.; Du, M.-H.; Melcher, C.; Shirwadkar, U.; Glodo, J.; Van Loef, E.; Shah, K.; Zhuravleva, M. Crystal growth and scintillation properties of pure and Tl-doped Cs3Cu2I5. *Nucl. Instrum. Methods Phys. Res., Sect. A* **2021**, *991*, No. 164963.
(39) Yuan, D. Air-Stable Bulk Halide Single-Crystal Scintillator Cs3Cu2I5 by Melt Growth: Intrinsic and Tl Doped with High Light Yield. *ACS Appl. Mater. Interfaces* **2020**, *12* (34), 38333−38340.
(40) Lian, L.; Zheng, M.; Zhang, W.; Yin, L.; Du, X.; Zhang, P.; Zhang, X.; Gao, J.; Zhang, D.; Gao, L.; et al. Efficient and Reabsorption-Free Radioluminescence in Cs3Cu2I5 Nanocrystals with Self-Trapped Excitons. *Adv. Sci.* **2020**, *7* (11), No. 2000195.
(41) Wang, Q.; Zhou, Q.; Nikl, M.; Xiao, J.; Kucerkova, R.; Beitlerova, A.; Babin, V.; Prusa, P.; Linhart, V.; Wang, J.; et al. Highly Resolved X-Ray Imaging Enabled by In(I) Doped Perovskite-Like Cs3Cu2I5 Single Crystal Scintillator. *Adv. Opt. Mater.* **2022**, *10* (11), No. 2200304.
(42) Glodo, J.; van Loef, E. V. D.; Koschan, M.; Zhuravleva, M.; Melcher, C. L.; Shah, K. In *Cs3Cu2I5:Tl,Li − Dual Mode Scintillator*, 2021 IEEE Nuclear Science Symposium and Medical Imaging Conference, Virtual; IEEE, 2021.
(43) Wang, Q.; Wang, C.; Wang, Z.; Sun, X.; Nikl, M.; OuYang, X.; Wu, Y. Achieving Efficient Neutron and Gamma Discrimination in a Highly Stable 6Li-Loaded Cs3Cu2I5 Perovskite Scintillator. *J. Phys. Chem. Lett.* **2022**, *13* (39), 9066−9071.
(44) Xiang, P.; Wei, Q.; Wang, C.; Cai, P.; Tong, Y.; Tang, G.; Sun, X.; Yang, F.; Shi, H.; Liu, Z.; Qin, L. An all-inorganic Li-doped Cs3Cu2I5 single crystal for dual gamma ray and neutron detection applications. *J. Mater. Chem. C* **2022**, *10* (41), 15400−15407.
(45) Shannon, R. D. Revised effective ionic radii and systematic studies of interatomic distances in halides and chalcogenides. *Acta Crystallogr., Sect. A* **1976**, *32* (5), 751−767.
(46) Toby, B. H.; Von Dreele, R. B. GSAS-II: the genesis of a modern open-source all purpose crystallography software package. *J. Appl. Crystallogr.* **2013**, *46* (2), 544−549.
(47) de Haas, J. T. M.; Dorenbos, P. Advances in yield calibration of scintillators. *IEEE Trans. Nucl. Sci.* **2008**, *55* (3), 1086−1092.
(48) Moszynski, M.; Bizard, G.; Costa, G. J.; Durand, D.; El Masri, Y.; Guillaume, G.; Hanappe, F.; Heusch, B.; Huck, A.; Peter, J.; et al. Study of n-γ discrimination by digital charge comparison method for a large volume liquid scintillator. *Nucl. Instrum. Methods Phys. Res., Sect. A* **1992**, *317* (1), 262−272.
(49) Werner, C. J.; Armstrong, J.; Brown, F.; Bull, J.; Casswell, L.; Cox, L.; Dixon, D.; Forster, R., III; Goorley, J.; Hughes, H., III; Favorite, J.; Martz, R.; Mashnik, S.; Rising, M.; Solomon, C.; Sood, A.; Sweezy, J.; Zukaitis, A.; Anderson, C.; Elson, J.; Durkee, J.; Johns, R.; McKinney, G.; McMath, G.; Hendricks, J.; Pelowitz, D.; Prael, R.; Booth, T.; James, M.; Fensin, M.; Wilcox, T.; Kiedrowski, B. C. *MCNP User's Manual Code Version 6.2*, LA-UR-17-29981; Los Alamos National Laboratory: Los Alamos, NM, USA, 2017.
(50) Harrison, M. J.; Graebner, A. P.; McNeil, W. J.; McGregor, D. S. Carbon coating of fused silica ampoules. *J. Cryst. Growth* **2006**, *290* (2), 597−601.
(51) Yip, L. S.; Shih, I.; Champness, C. H. Method of avoiding ampoule adhesion of ingots in Bridgman growth of CuInSe2. *J. Cryst. Growth* **1993**, *129* (1), 102−106.
(52) Wojakowska, A.; Krzyżak, E. Factorsaffecting the general shape of the phase diagram and compound formation inthe binary copper(I) halide−alkali-metal halide systems. *J. Therm. Anal. Calorim.* **2006**, *83* (3), 597−601.
(53) Wojakowska, A.; Górniak, A.; Kuznetsov, A. Y.; Wojakowski, A.; Josiak, J. Phase Diagram of the System Copper(I) Iodide + Cesium Iodide. *J. Chem. Eng. Data* **2003**, *48* (3), 468−471.
(54) Bigalke, K. P.; Hans, A.; Hartl, H. Synthese und Strukturuntersuchungen von Iodocupraten(I). IX. Synthese und Kristallstrukturen von Cs3Cu2I5 und RbCu2I3. *Z. Anorg. Allg. Chem.* **1988**, *563* (1), 96−104.
(55) Hull, S.; Berastegui, P. Crystal structures and ionic conductivities of ternary derivatives of the silver and copper monohalides—II: ordered phases within the (AgX)x−(MX)1−x and (CuX)x−(MX)1−x (M = K, Rb and Cs; X = Cl, Br and I) systems. *J. Solid State Chem.* **2004**, *177* (9), 3156−3173.
(56) Li, K.-N.; Zhang, X.-P.; Gui, Q.; Jin, P.; Tian, G. Characterization of the new scintillator $Cs_2LiYCl_6:Ce^{3+}$. *Nucl. Sci. Tech.* **2018**, *29* (1), No. 11.
(57) Glodo, J.; Wang, Y.; Shawgo, R.; Brecher, C.; Hawrami, R. H.; Tower, J.; Shah, K. S. New Developments in Scintillators for Security Applications. *Phys. Procedia* **2017**, *90*, 285−290.
(58) Yang, K.; Menge, P. R.; Lejay, J.; Ouspenski, V. In *Scintillation Properties and Temperature Responses of* $Cs_2LiLaBr_6:Ce^{3+}$, 2013 IEEE Nuclear Science Symposium and Medical Imaging Conference (2013 NSS/MIC); IEEE, 2013; pp 1−6.
(59) Han, D.; Shi, H.; Ming, W.; Zhou, C.; Ma, B.; Saparov, B.; Ma, Y.-Z.; Chen, S.; Du, M.-H. Unraveling luminescence mechanisms in zero-dimensional halide perovskites. *J. Materials Chem. C* **2018**, *6* (24), 6398−6405.
(60) Du, M.-H. Emission Trend of Multiple Self-Trapped Excitons in Luminescent 1D Copper Halides. *ACS Energy Lett.* **2020**, *5* (2), 464−469.
(61) Lam, S.; Swider, S.; Fiala, J.; Datta, A.; Motakef, S. Microscale luminescence imaging of defects, inhomogeneities, and secondary phases in halide scintillators. *Nucl. Instrum. Methods Phys. Res., Sect. A* **2015**, *784*, 23−28, DOI: 10.1016/j.nima.2014.12.038.

https://doi.org/10.1021/acsaelm.4c02245
ACS Appl. Electron. Mater. XXXX, XXX, XXX−XXX

(62) Onken, D. R.; Gridin, S.; Williams, R. T.; Williams, C. B.; Donati, G. L.; Gayshan, V.; Vasyukov, S.; Gektin, A. Investigating the origins of double photopeaks in CsI:Tl samples through activator mapping. *Nucl. Instrum. Methods Phys. Res., Sect. A* **2018**, *893*, 151−156.
(63) Ren, G.; Chen, X.; Lu, S.; Li, Z.; Xue, X.; Shen, D. Non-uniformity of light output in large-sized CsI(Tl) crystals grown by non-vacuum Bridgman method. *Nucl. Instrum. Methods Phys. Res., Sect. A* **2006**, *564* (1), 364−369.
(64) van Goethem, M. J.; Wallace, M. S.; Nett, B. E.; Famiano, M. A.; Herner, K. R.; Oostdyk, D. J.; Mocko, M.; Lynch, W. G.; Tsang, M. B.; Schotanus, P.; et al. Investigations and corrections of the light output uniformity of CsI(Tl) crystals. *Nucl. Instrum. Methods Phys. Res., Sect. A* **2004**, *526* (3), 455−476.
(65) Belsky, A.; Garnier, N.; Dujardin, C.; Pedrini, C.; Varrel, B.; Chevallier, P.; Firsov, A. In *The Effect of Thallium Distribution on Luminescence of CsI: Tl*, Proceeding of the Seventh international Symposium on Physics and Chemistry of Luminescence materials; Electrochemical Society, 1998.
(66) Trefilova, L. N.; Kudin, A. M.; Kovaleva, L. V.; Zaslavsky, B. G.; Zosim, D. I.; Bondarenko, S. K. Concentration dependence of the light yield and energy resolution of NaI:Tl and CsI:Tl crystals excited by gamma, soft X-rays and alpha particles. *Nucl. Instrum. Methods Phys. Res., Sect. A* **2002**, *486* (1), 474−481.
(67) Wang, J.; Wang, Q.; Li, H.; Shi, J.; Xiu, H.; Ren, G.; Wu, Y. Segregation effects of Tl and Li ions on the scintillation properties of NaI:Tl,Li single crystals. *J. Cryst. Growth* **2023**, *612*, No. 127199.
(68) West, J. B. A theoretical model for the migration of energy from the particle track in an inorganic scintillator. *J. Phys. B: At. Mol. Phys.* **1970**, 3 (12), No. 1692.
(69) Gwin, R.; Murray, R. B. Scintillation Process in CsI(Tl). I. Comparison with Activator Saturation Model. *Phys. Rev.* **1963**, *131* (2), 501−508.
(70) Murtagh, C.; Klemic, G.; Karam, P. A.; Goldhagen, P. *Mobile Radiation Detection Systems Market Survey Report*, National Urban Security Technology Laboratory, U.S. Department of Homeland Security, Science and Technology Directorate, 2023.

https://doi.org/10.1021/acsaelm.4c02245
ACS Appl. Electron. Mater. XXXX, XXX, XXX−XXX